

# MHD supernova explosions – Large-scale magnetic field effects

CETIN C. EVIRGEN<sup>1</sup> AND FREDERICK A. GENT<sup>2</sup>

<sup>1</sup>*School of Mathematics, Statistics and Physics, Newcastle University Newcastle upon Tyne, NE1 7RU, UK*

<sup>2</sup>*ReSoLVE Centre of Excellence, Department of Computer Science, Aalto University, Aalto, PO Box 15400, FI-00076, Finland*

(Received Jun 2019; Revised –; Accepted –)

Submitted to ApJ

## ABSTRACT

We examine the effect of uniform ambient magnetic fields on the evolution of supernova-driven blast waves into a homogeneous ambient ISM in thermal equilibrium. Using the PENCIL CODE we simulate high resolution nonideal magnetohydrodynamic simulations in 3D. We find that supernova blast waves *are* sensitive to plane-parallel magnetic fields of strength in excess of  $1\ \mu\text{G}$  for ambient gas number density  $1\ \text{cm}^{-3}$ . Perpendicular to the field, the inward magnetic pressure gradient induces retrograde mass accretion in the wake of the primary shock front. Subsequently, we find that the primary shockwave expands faster perpendicular to the field, but with reduced momentum, while the remnant core is subject to magnetic confinement. This leads to a decrease in fractional volume of hot gas but also an increase in the density and temperature of hot gas in the magnetically confined remnant. The magnetic pressure gradient behind the shock front generates enhanced regions favourable to UV-heating and thus reduces net radiative losses. Although the presence of a strong uniform magnetic field can reduce momentum early on, and hence residual kinetic energy, it increases the efficiency of residual total energy injection by the SN into the ISM by up to 40% within 1 Myr.

**Keywords:** (stars:)supernovae: individual — ISM: supernova remnants — magnetohydrodynamics (MHD)

## 1. INTRODUCTION

Supernova explosions (SNe) play a significant role in galactic dynamics. They provide pressure support and inject energy, driving turbulence and large-scale outflows (McKee & Ostriker 1977; Chevalier & Clegg 1985; Mac Low & Klessen 2004; Murray et al. 2005; Girichidis et al. 2016). Isolated SNe can significantly impact their local ambient environment, whether evacuating or fragmenting a dense molecular cloud from within, or expansion into, and advection through, less dense hot gas regions. Clusters of SN can form larger hot gas structures (superbubbles or chimneys), spanning typically hundreds of parsec, and feeding the galactic fountain.

Both individual SNe and SNe clusters, such as superbubbles arising from OB associations, have been studied analytically (Taylor 1950; Sedov 1959; Tomisaka et al. 1981; Cioffi et al. 1988) and numerically (Chevalier 1974; Ferriere et al. 1991; Slavin & Cox 1992; Jun & Norman 1996; Tomisaka 1998; Caunt & Korpi 2001; Hanayama &

Tomisaka 2006; Zirakashvili & Ptuskin 2008; Kim & Ostriker 2015; Yadav et al. 2017). SNe evolution is spherically symmetric in a non-magnetized uniform ambient ISM (Spitzer 1978; Cioffi et al. 1988). From a 1D model Chevalier (1974) concluded that if the postshock magnetic pressure does not exceed the ram pressure, then the magnetic field does not affect the SN remnant dynamics, other than the thickness of its shell. Further, from 3D ideal magnetohydrodynamic (MHD) simulations Kim & Ostriker (2015) conclude that the final momentum injected by an SNe is insensitive to the the magnetic field, although if the ambient plasma- $\beta$  is greater than 1 the late stage remnant temperature is affected. Hanayama & Tomisaka (2006) show that strong plane-parallel magnetic fields can inhibit the expansion of individual SN remnants perpendicular to the magnetic field, thus altering the aspect ratio of the remnant and leading to a deviation from the spherical expansion typical of hydrodynamic (HD) remnants. Caunt & Korpi (2001) show the expansion profile for an individual SN remnant in a magnetized medium, with the blast wave expanding faster perpendicular to a uniform, plane-parallel magnetic field. While the results of Hanayama & Tomisaka (2006) and Caunt & Korpi (2001) seem to disagree, we

aim to show that they instead describe complimentary aspects of MHD remnant expansion.

In this Paper, we focus on understanding the role of a large-scale magnetic field in simulations of SN remnants in an idealised physical setup. Our initial aim is twofold: to examine the effects of large-scale magnetic fields in isolation, and to assess the claim that large-scale magnetic fields do not affect momentum injection in SN remnants. In order to make direct comparison, we use similar parameters to numerical models from earlier studies.

SN explosions are a major component of larger-scale numerical models of galaxies, evolving turbulence in which SN remnants are more realistically embedded. However, these models are typically too coarse to resolve SN remnants self-consistently. Remnant-scale modelling provides necessary constraints on the critical aspect of energy injection to apply in the larger simulations. However, a less idealized model will ultimately be required for comparison with SN remnant observations. We shall develop such models in an incremental and cumulative manner in subsequent studies.

In Section 2 we present details of the numerical model. We then discuss magnetic effects on the aspect ratio of SN remnants in Section 3. This is followed examination of the effect of large-scale magnetic fields on momentum injection by SN remnants in Section 4. In Section 5 we discuss magnetic effects on the thermodynamical properties of SN remnants. Residual energy injection by the remnants into the ISM is measured in Section 6 and we consider the critical magnetic field strength for MHD effects to become important in Section 7. We present a summary and discussion of our results in Section 8.

As a sanity check we compute some shock-tube experiments and other related tests, which verify our qualitative results are not sensitive to numerical recipes or parameters. These are external to the focus of the paper so we include them in an Appendix. In Appendix A, we discuss the effect of physical parameters on 1D HD and MHD shocks. Appendix B provides a preliminary set of results on the effects of large-scale magnetic fields on 1D shocks in ambient gas densities ranging from  $n = 10^{-2} \text{ cm}^{-3}$  to  $n = 10^{-2} \text{ cm}^2$ . Appendix C examines the effect of changing ambient gas temperature in 3D simulations of SN explosions.

## 2. NUMERICAL METHODS

Here we explore further the MHD effects, especially momentum injection, the anisotropy of the remnant, and effects on the gas and density distribution within the remnant. We use the Pencil Code<sup>1</sup>, adapted for highly compressible nonideal MHD turbulence.

<sup>1</sup> <https://github.com/pencil-code>

The MHD equations applied include the compressible form of the continuity equation

$$\frac{D\rho}{Dt} = +\dot{\rho}_{\text{SN}} - \rho \nabla \cdot \mathbf{u} + \zeta_D \nabla^2 \rho + \nabla \zeta_D \cdot \nabla \rho, \quad (1)$$

where  $\rho$  is the gas density and  $\dot{\rho}_{\text{SN}}$  is the mass of the SN ejecta, which for the purposes of these experiments is set to zero. An artificial shock dependant mass diffusion,  $\zeta_D$ , is required for numerical stability in simulations of the SN-driven turbulent ISM.  $\zeta_D \propto f_{\text{shock}}$ , where

$$f_{\text{shock}} = \left\langle \max_5 [(-\nabla \cdot \mathbf{u})_+] \right\rangle (\min(\Delta x, \Delta y, \Delta z))^2. \quad (2)$$

This is described in Gent et al. (2019), along with shock dependant diffusivities included in the following equations. The material derivative is

$$\frac{D}{Dt} = \frac{\partial}{\partial t} + \mathbf{u} \cdot \nabla.$$

The momentum equation evolving velocity,  $\mathbf{u}$ , includes an artificial shock dependent viscosity,  $\zeta_\nu$  and a momentum conserving correction term for  $\zeta_D$  from Equation (1). The pressure force is expressed in terms of specific entropy,  $s$ , specific heat capacity of the gas at constant pressure,  $c_p$ , and sound speed,  $c_s$ , yielding

$$\rho \frac{D\mathbf{u}}{Dt} = -c_s^2 \rho \nabla \left( \frac{s}{c_p} + \ln \rho \right) + \nabla \cdot (2\rho \nu \nabla \mathbf{S}) + \mathbf{j} \times \mathbf{B} + \rho \nabla (\zeta_\nu \nabla \cdot \mathbf{u}) - \mathbf{u} (\zeta_D \nabla^2 \rho + \nabla \zeta_D \cdot \nabla \rho). \quad (3)$$

This also includes the Lorentz force due to the magnetic field,  $\mathbf{B}$ , and the current density,  $\mathbf{j} = \mu_0^{-1} \nabla \times \mathbf{B}$ . The vacuum magnetic permeability is denoted  $\mu_0$ . Viscous stresses are accounted for through the shear viscosity  $\nu$  within the divergence of the rate of strain tensor  $\mathbf{S}$ , defined by

$$2\mathbf{S}_{ij} = \frac{\partial u_i}{\partial x_j} + \frac{\partial u_j}{\partial x_i} - \frac{2}{3} \delta_{ij} \nabla \cdot \mathbf{u}, \quad \text{with} \quad \mathbf{S}^2 \equiv S_{ij} S_{ij}.$$

The energy equation is evolved in the form of the specific entropy with

$$\begin{aligned} \rho T \frac{Ds}{Dt} = & \dot{\sigma}_{\text{SN}} + \rho \Gamma - \rho^2 \Lambda + 2\rho \nu \mathbf{S}^2 + \eta \mu_0 |\mathbf{j}|^2 \\ & + \nabla \cdot (c_p [\chi + \zeta_\chi] \rho \nabla T) \\ & - c_v T (\zeta_D \nabla^2 \rho + \nabla \zeta_D \cdot \nabla \rho), \end{aligned} \quad (4)$$

where  $T$  denoted the gas temperature and  $c_v$  the specific heat capacity of the gas at constant volume. Heat sources and sinks include SN explosion thermal energy,  $\dot{\sigma}_{\text{SN}} = 10^{51} \text{ erg}$  at time  $t = 0$ , and viscous and Ohmic heating, in which  $\eta$  denotes the resistivity. As applied in Gent et al. (2013), the radiative cooling,  $\Lambda$ , applies Wolfire et al. (1995) at lower temperatures and Sarazin

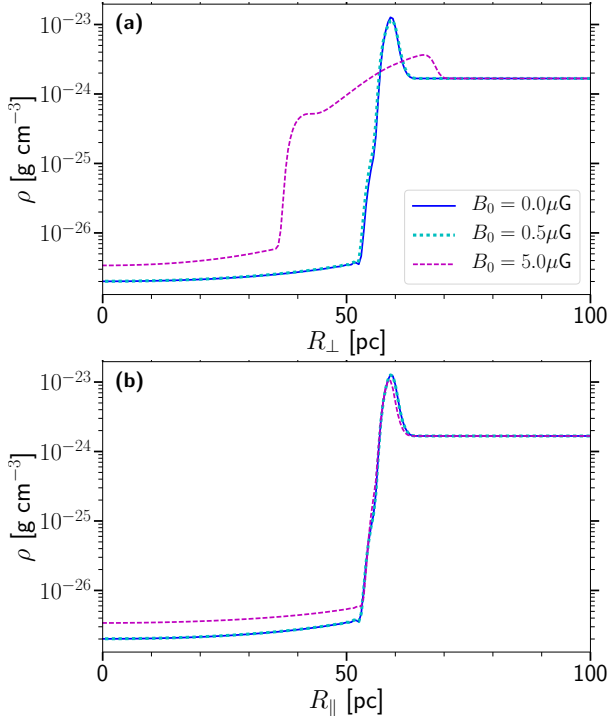


**Figure 1.** Radial profiles of gas density (a) perpendicular and (b) parallel to the magnetic field at  $t = 1$  Myr.

& White (1987) for the hot gas. Diffuse UV-heating,  $\Gamma$ , follows Wolfire et al. (1995). Thermal conductivity,  $\chi$  and shock dependant  $\zeta_\chi$  are applied, and an energy conserving correction term due to  $\zeta_D$  from Equation (1).

The induction equation is solved in terms of the vector potential,  $\mathbf{A}$ , which conserves  $\nabla \cdot \mathbf{B} = 0$  by design. In contrast to the previous equations we do not include any shock capturing resistivity, as this has the unphysical effect of suppressing magnetic field in the SN remnant shell through excessively rapid diffusion (reconnection). However, we are interested in investigating the nature of dynamo in the turbulent ISM, so isotropic resistivity is included to yield

$$\frac{\partial \mathbf{A}}{\partial t} = \mathbf{u} \times \mathbf{B} + \eta \nabla^2 \mathbf{A} + \nabla \cdot \mathbf{A} \nabla \eta. \quad (5)$$

The system of equations is completed by the ideal gas equation of state with adiabatic index  $\gamma = c_p/c_v = 5/3$ . The monatomic gas with hydrogen and helium abundances representative of the Solar neighbourhood of the Milky Way has mean molecular weight 0.531 when assumed to be fully ionised. A comprehensive description of the Pencil Code application to SN driven ISM turbulence is given in Gent (2012, Chapter 3), while the further enhancement of shock handling and stability methods for reproducing SN blast waves in HD are presented in Gent et al. (2019).

Here, we consider a plane-parallel uniform magnetic field  $\mathbf{B} = (0, B_0, 0)$ , for  $B_0 \in [0, 5] \mu\text{G}$ . With a fiducial

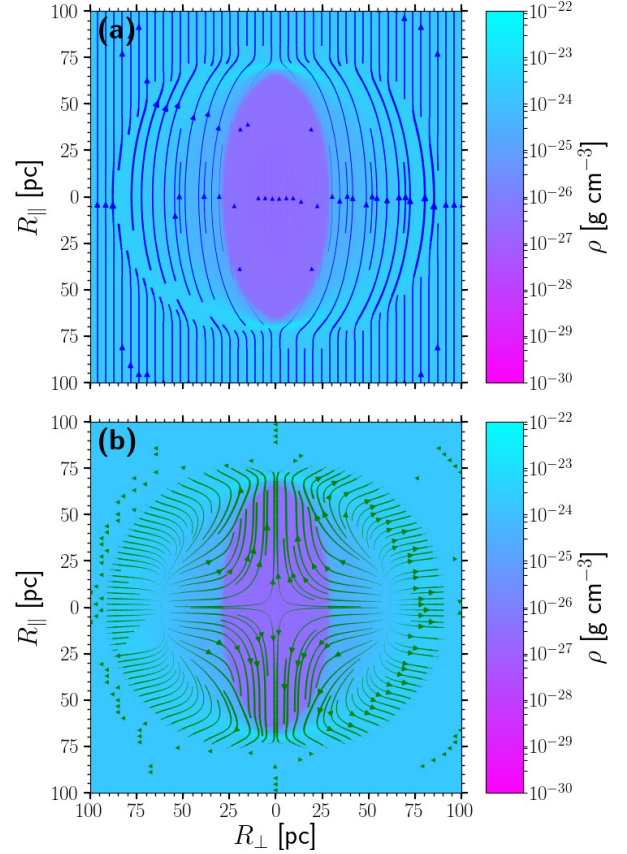


**Figure 2.** Cross-section of the strongly magnetized remnant at 2 Myr, with (a) magnetic field lines and (b) velocity stream lines overlaid. Line thickness is proportional to field strength.

gas number density,  $n_0$ , for the ambient ISM of  $1 \text{ cm}^{-3}$  and resolution 0.5 parsec along each side, we use a Cartesian grid of  $528^2$  by  $576$  parallel to the field. For consistent thermal pressure in the ambient ISM throughout the duration of the model blastwaves we set a thermal equilibrium temperature of  $T \simeq 260 \text{ K}$ .

The numerical model uses constant magnetic resistivity,  $\eta = 8 \cdot 10^{-4} \text{ kpc km s}^{-1}$  and sound speed dependent viscosity,  $\nu = \nu_0 c_s$ , where  $\nu_0 = \Delta x = 5 \cdot 10^{-4} \text{ kpc}$  is the grid resolution, and  $c_s$  is the speed of sound. A test of alternate Prandtl numbers produced qualitatively similar solutions, and results were convergent with resolution of 0.5 pc, other than a thinner more dense remnant shell.

### 3. SN REMNANT ASPECT RATIO

We show the radial profiles at 1 Myr of gas density in Figure 1, perpendicular to the magnetic field, Panel (a), and parallel, (b), for models with  $B_0 = 0, 0.5$  and  $5 \mu\text{G}$ . With a weak magnetic field  $B_0 \leq 0.5 \mu\text{G}$ , the evolution of the remnant is very similar to the HD model. With stronger  $B_0$  the remnant core is less diffuse, and the slightly less dense remnant shell parallel to the field is coincident with the HD model shell. However, perpen-

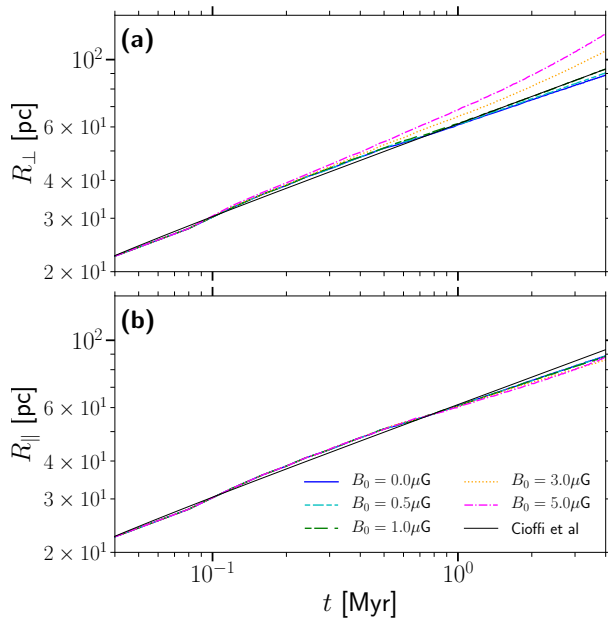


**Figure 3.** SN remnant radius,  $R_{\perp}$ , perpendicular and  $R_{\parallel}$ , parallel to  $B_0$ . Numerical solutions are compared to the HD analytical solution (Cioffi et al. 1988).

dicular to the field the mass profile of the remnant is substantially altered. Mass is more confined within the remnant, but Figure 1 also shows that the SN shockwave propagates faster perpendicular to the magnetic field while carrying less mass at the shock front.

Figure 2(a) shows the shockwave at 2 Myr compressing magnetic field lines to form a dense magnetic collar. Magnetic field is initially evacuated from the core of the remnant. It is evident that the MHD remnant core geometry resembles a prolate spheroid with the polar radius parallel to the magnetic field. The ratio of polar to equatorial radius increases with field strength. In contrast, the remnant shock front forms the surface of an oblate spheroid with equatorial radius perpendicular to the magnetic field. This ratio of polar to equatorial radius decreases with field strength.

Figure 2(b) shows the structure of flows driven by the remnant in a strongly magnetized ambient ISM. The shockwave drives outward flows as expected. We find inward flows of comparable speed to the outward flows. There are retrograde shocks towards the core in all the models, but for the HD and weakly magnetic models these carry negligible mass. For strong  $B_0$  the magnetic forces drive inward gas flow from the shell, perpendicular to the magnetic field. As the flow approaches the thermally dominated core, the outward thermal pressure gradient channels the flows parallel to the magnetic field, creating a quadrupolar velocity field between the shockwave and core. In the HD and weakly magnetized remnants, the internal gas flows of the remnant remain radially outward.

By 2 Myr the magnetic field along with some of the gas, has filled almost half the remnant void behind the shock front. This forms an inter-shock region between the core of the remnant and its shell. At even later times the field strength throughout the inter-shock region is close to its original strength. The gas in the core remains hot and diffuse, with magnetic field strength considerably weaker than outside the core.

Figure 3 shows the radial evolution of the shockwave for the HD, weakly magnetized and strongly magnetized remnants. The HD remnant has a single characteristic length; the shockwave radius, since the shockwave and core are coupled. This shows good agreement with the analytical solution of Cioffi et al. (1988) for a spherically symmetric model. Shock wave radii are near identical for all models, parallel to the magnetic field. The weakly magnetized remnant behaviour in Figure 3 closely resembles that of the HD remnant. However, perpendicular to the strongly magnetized field the shockwaves diverge from the other profiles near  $t = 100$  kyr and propagate faster.

Given the ubiquity of magnetic fields in the ISM, it is reasonable to anticipate spheroid morphology to be common in SN remnants. This may be useful in understanding the 3D structure of observed remnants. For example, G351.0-5.4, discovered in de Gasperin et al. (2014) is modelled in first approximation as spherical. This may be reasonable for observations of the shell, which from our models appears only slightly oblate, but misleading for the remnant core. Alternatively, comparisons of gamma-ray and radio data around remnant W44 (Cardillo et al. 2014) indicate a smaller spheroid in gamma-ray emission with polar radius offset from the surrounding spheroid in radio emission, and the presence of magnetic field in the shock  $B \geq 10^2 \mu\text{G}$ . Complex interaction with molecular clouds and the turbulent ISM affect the morphology of the remnant, but the inter-shock region may also be part of the explanation for the misalignment in the observational profiles.

Modelling the local bubble of the Milky Way with a prolate sphere Alves et al. (2018) find this a reasonable fit even for the magnetic shell. In contrast to our findings, they determine the remnant field to be vertical, out of alignment to the neighbourhood galactic field, and highly anisotropic between North and South. Perhaps, however, an oblate spheroid shell with polar axis parallel to the galactic plane would be an alternative model consistent with the galactic magnetic field.

Any speculation about how our results relate to observational features, are of course at this stage highly tentative. The large scale alignment of magnetic fields in the ISM will surely not be uniform on scales of a few parsecs. The structure of the turbulent magnetic field, the stratification and inhomogeneity of the gas density and temperature, and the turbulent motion of the ambient ISM will be considered in future work, let alone the effects of chemistry and ionization on the observational



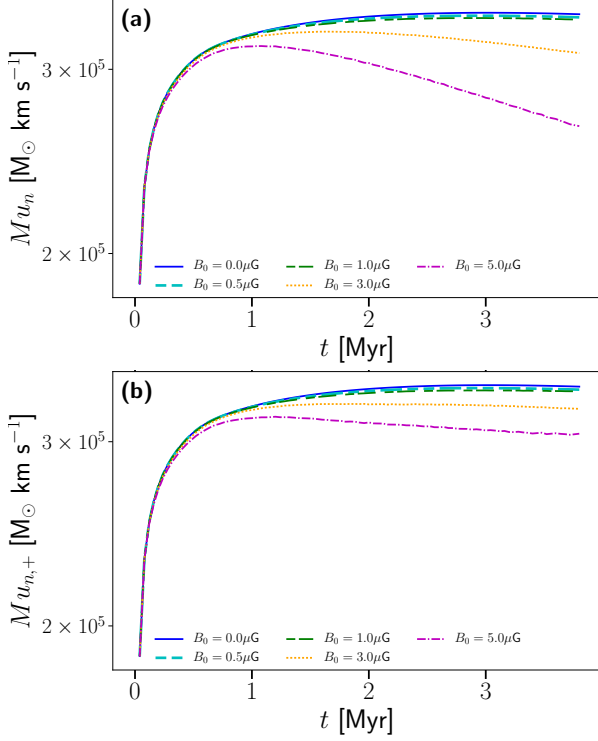


**Figure 4.** Time evolution of (a) total and (b) outward momentum injection for a number of SN models with magnetic field strengths  $B_0 \in [0, 5] \mu\text{G}$ . Momentum, at a given snapshot, is calculated as  $\int_{\text{SNR}} \rho(\mathbf{u} \cdot \hat{\mathbf{n}}) dV$ , where  $\hat{\mathbf{n}}$  is the radial unit vector from the centre of the SN explosion. The scatter plots with blue star and magenta circle symbols show outward momentum injection for the HD model and strongly magnetized model ( $B_0 = 5 \mu\text{G}$ ), respectively.

signatures. Anisotropy of SN remnants may of course also arise independent of magnetic effects.

#### 4. MOMENTUM INJECTION

In a typical HD supernova explosion, the propagation of the shock, and subsequent momentum injection into the surrounding medium, is dominated by the thermal pressure gradients, which evacuate mass from the core into the blastwave. In a very similar physical set up to ours, Kim & Ostriker (2015) find the SN terminal momentum injection to be about  $4 \times 10^5 M_\odot \text{ km s}^{-1}$ , defined by

$$Mu_n = \int_V \rho(\mathbf{u} \cdot \hat{\mathbf{n}}) dV, \quad (6)$$

where  $\hat{\mathbf{n}}$  is the radial unit vector from the centre of the SN explosion.

We consider this calculation with a modification to account for non-spherical expansion of the SN remnant. The most general approach would be to adopt a tri-axial ellipsoid profile. However in this case, the remnants have two distinct length scales, the SNR radius parallel and perpendicular to the magnetic field,  $R_\parallel$  and  $R_\perp$ ,

respectively. This change produces a bi-axial ellipsoidal remnant, rather than the spherical HD remnants. The ellipsoidal surface is represented by

$$g(\mathbf{x}) = \left(\frac{x}{R_\perp}\right)^2 + \left(\frac{y}{R_\parallel}\right)^2 + \left(\frac{z}{R_\perp}\right)^2, \quad (7)$$

where  $x$  and  $z$  are the directions perpendicular to the magnetic field, and  $y$  is parallel to the magnetic field. Here  $g(\mathbf{x}) = 1$  represents the remnant shell.<sup>2</sup> We now define the normal to the shell as

$$\hat{\mathbf{n}} = \frac{\nabla g}{|\nabla g|},$$

where

$$\nabla g = \left( \frac{2x}{R_\perp^2}, \frac{2y}{R_\parallel^2}, \frac{2z}{R_\perp^2} \right).$$

It can be shown that  $R_\perp = R_\parallel$  leads to a spherical remnant profile and  $\hat{\mathbf{n}} = \hat{\mathbf{x}}$ .

With this definition for  $\hat{\mathbf{n}}$  applied to Equation (6), we obtain total momentum injection  $3.3 \times 10^5 M_\odot \text{ km s}^{-1}$  for the HD remnant, similar to Kim & Ostriker (2015). we plot the evolution of total momentum for the HD and a range of MHD remnants in Figure 4(a). As the thermal pressure gradient reduces in the remnant the pressure driven snowplough (PDS) transitions to the momentum conserving snowplough (MCS), as described by Cioffi et al. (1988). It can be seen that MCS for the HD model initiates a little later than 2 Myr. A transient MCS occurs much earlier ( $t \simeq 1 \text{ Myr}$ ) for the strongly magnetized model, subsequently losing momentum thereafter. As it might be argued that only the outward momentum drives the ISM turbulence we also calculate the outward momentum injection,  $Mu_n|_+$ , which is plotted in Figure 4(b).

There is a negligible difference between the HD and weak MHD models, but for magnetic field strength above  $1 \mu\text{G}$  the momentum injection diverges significantly from the HD. Contrasting panels (a) and (b) it is evident that although HD remnants feature retrograde shocks, these carry negligible mass back towards the core, while there is significant inward momentum for the strong MHD shocks.

Kim & Ostriker (2015) find that momentum injection ceases within two to three shell-forming times, before the magnetic energy becomes comparable to the thermal energy in the shell. Subsequently, they argue that magnetic effects will not lead to further momentum injection by the remnant. However, from both panels in Figure 4 we find our strong MHD solutions ( $B_0 = 3.0, 5.0 \mu\text{G}$ ) diverge from the HD solution within 200 kyr. These show non-monotonic evolution, reaching a local maximum ( $3.1 \times 10^5 M_\odot \text{ km s}^{-1}$ ) after 700 kyr followed by

<sup>2</sup>  $g(\mathbf{x}) = k$ , where  $0 \leq k \leq 1$ , represent contours of the remnant.

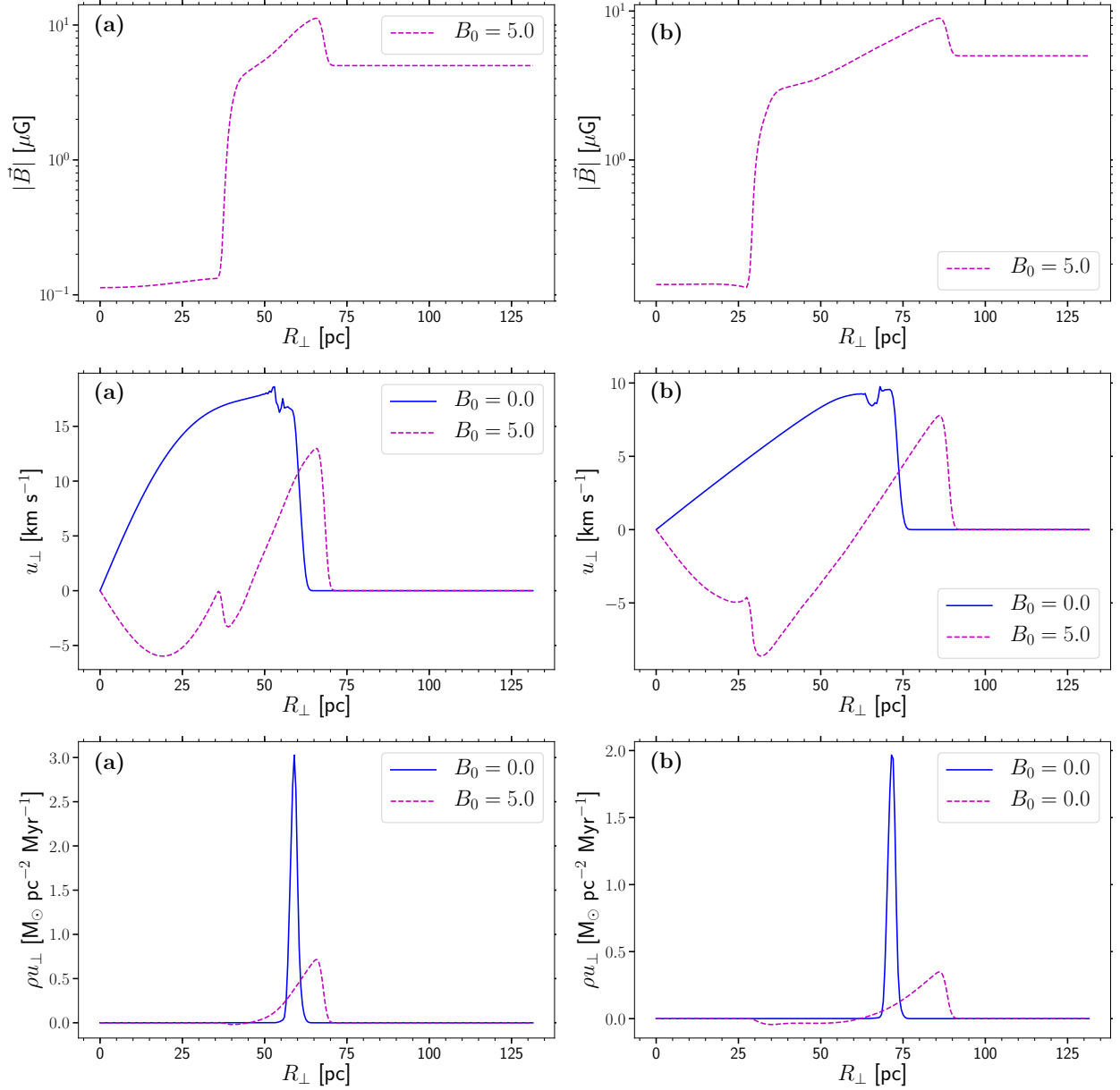


**Figure 5.** Radial profiles perpendicular to the magnetic field at (a) 1 Myr and (b) 2 Myr of magnetic field strength (top), velocity and momentum (bottom).

decay. However, outward momentum injection becomes steady after 2 Myr and levels off at  $3 \times 10^5 \text{ M}_\odot \text{ km s}^{-1}$ . This suggests that momentum injection is reduced by up to 10% in the presence of a large-scale plane-parallel uniform magnetic field. Evirgen et al. (2019) show that a  $B_{\text{rms}} \sim 3 \mu\text{G}$  dynamo-evolved magnetic field, featuring a strong locally plane-parallel large-scale coherent structure, leads to a decrease in vertical velocity profile. An important contributing factor could be suppression of momentum injection at the SN forcing scale, as seen here.

To illustrate what is changing due to the strong MHD we show radial profiles perpendicular to the magnetic

field at 1 Myr and 2 Myr in panels (a) and (b), respectively in Figure 5 of the magnetic field strength (top), velocity (centre) and momentum (bottom).

Momentum in the shell of the HD remnant is a factor of 4–6 higher and centered narrowly about the shock front. The MHD shock in all profiles is broader, projecting both in advance of the HD shock position and including an extended weak inward momentum behind the shock front. Even slowing below  $10 \text{ km s}^{-1}$  by 2 Myr the MHD blast wave still remains supersonic. We find that the blast wave remains supersonic even up to 4 Myr. We see from that the magnetic field is swept up into the

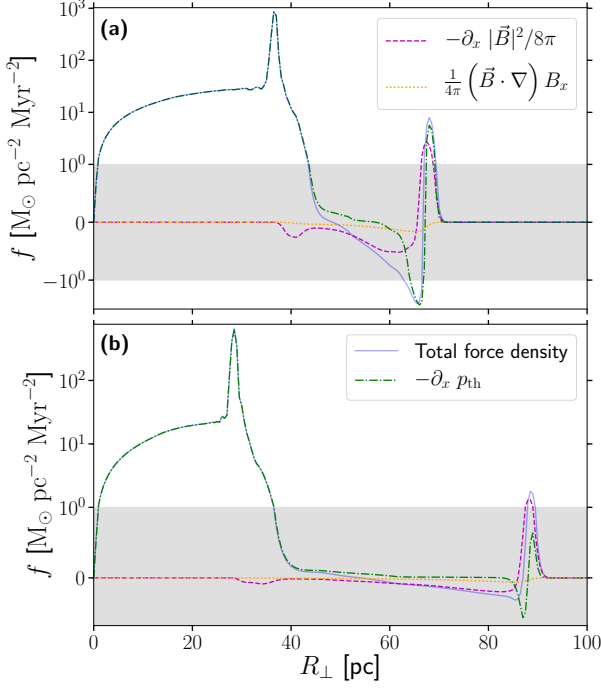


**Figure 6.** Force density,  $f$  perpendicular to magnetic field with  $B_0 = 5\mu\text{G}$  at  $t = 1\text{ Myr}$  (a) and  $t = 2\text{ Myr}$  (b). The vertical scale across the shaded area is linear and logarithmic elsewhere.

remnant shell, but that some of this relaxes back towards the core over time.

In order to explore what are the magnetic effects that increase the outward velocity, but inhibit the outward momentum of the MHD remnant in the latter stage, we consider the momentum equation perpendicular to  $B_0$ ,

$$\rho \frac{Du_\perp}{Dt} = -\frac{\partial}{\partial R_\perp} \left( p + \frac{|B|^2}{2\mu_0} \right) + \frac{1}{\mu_0} (\mathbf{B} \cdot \nabla) B_\perp + \mathcal{D}, \quad (8)$$

where  $p$  denotes thermal pressure and  $\mathcal{D}$  refers to diffusive terms in the equation. For our analysis, we are interested in the interaction between the pressure gradient terms and the magnetic tension term on the right hand side of the equation.

For the strong MHD model Figure 6 shows the forces applying perpendicular to  $B_0$  at  $t = 1\text{ Myr}$ , Panel (a) and  $t = 2\text{ Myr}$  (b). Interestingly, the very large thermal pressure gradient extending through the inner core to about 40 pc at 1 Myr is confined to only 30 pc by 2 Myr. A negative thermal pressure gradient does evolve into the wake of the shock, and this is true also for the HD remnant. However this is too remote from the core to account for its confinement late on. Magnetic effects gradually become dominant at the blastwave, primarily the magnetic pressure gradients, where the outward magnetic pressure gradient is comparable to the thermal gradient at  $t = 1\text{ Myr}$ , and 2–3 times greater at  $t = 2\text{ Myr}$ . However, the negative pressure gradient in

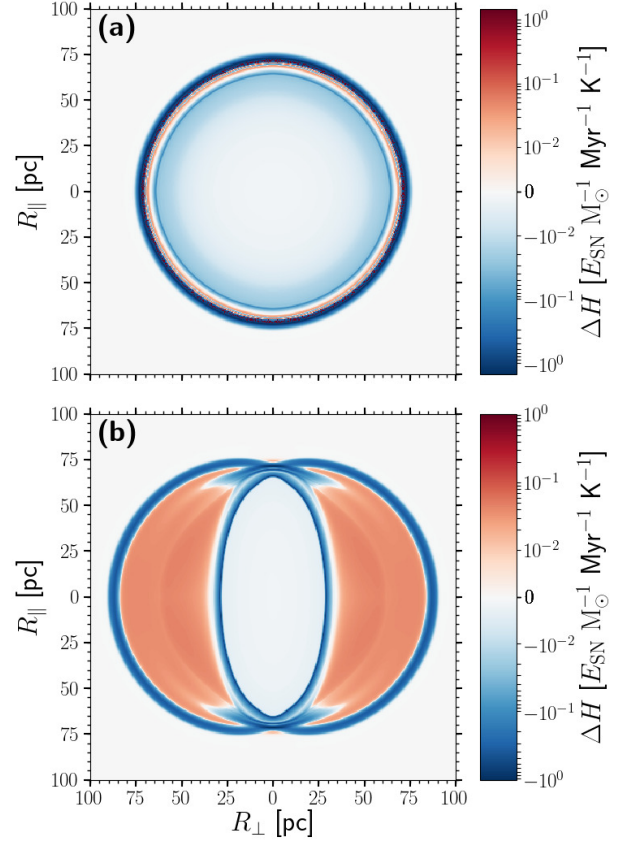


**Figure 7.** Cross sections at 2 Myr for the HD model, (a), and the model with  $B_0 = 5\mu\text{G}$ , (b), of the net heating,  $\Delta H = T^{-1}(\Gamma - \rho\Lambda)$ .

the wake of the shock appears to be the most interesting. The negative force applies throughout the *inter-shock region*, between the primary blast wave and the inner thermal pressure front. The magnetic pressure force peels mass away from the remnant shell and drives it inwards along with some of the magnetic field. This broadens the mass shell profile we see from Figure 1 and the magnetic field profile from Figure 5 (top panels) and provides the substantive forces confining the remnant core compared to HD. For most of the  $60 < R_\perp < 90\text{ pc}$  region by 2 Myr the magnetic pressure gradient dominates the thermal pressure gradient. Magnetic tension is subdominant perpendicular to the magnetic field.

## 5. THERMODYNAMICS OF MHD REMNANTS

The effect of confinement of the remnant core by the inward magnetic pressure gradient is to reduce adiabatic cooling compared to HD. The system is non-adiabatic, so how does the redistribution of mass in the strong MHD case affect its thermal properties? Snapshots of the net heating,  $\Delta H = T^{-1}(\Gamma - \rho\Lambda)$ , are presented in Figure 7 for the HD model, Panel (a), and strong MHD model, (b). In the HD and weak MHD models, cooling dominates everywhere in the remnant, except for a thin

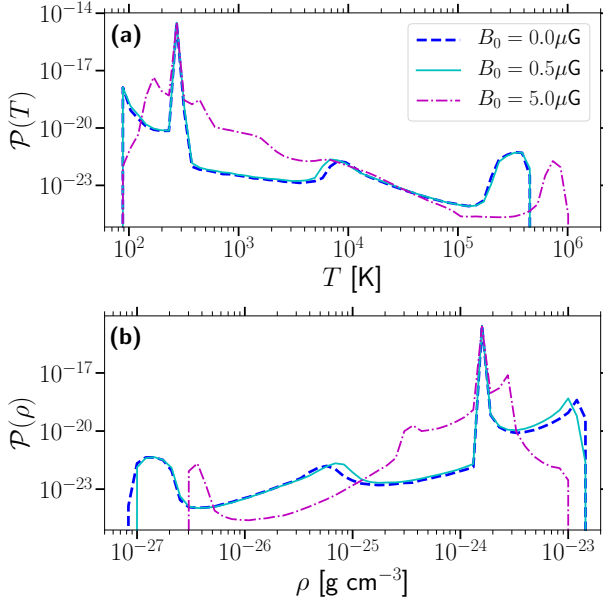


**Figure 8.** Mass-weighted probability density functions (PDFs) of (a) gas temperature and (b) gas density at 2.0 Myr for HD (dashed blue) and MHD models with  $B_0 = 0.5 \mu\text{G}$  (solid cyan) and  $B_0 = 5.0 \mu\text{G}$  (dash-dotted magenta) models.

layer just behind the cooling shell. In the strong MHD model cooling dominates in the confined remnant inner core and shell, but in the inter-shock region perpendicular to the field UV-heating exceeds radiative losses. In Figure 1 (a) this applies for  $35 \lesssim R_\perp \lesssim 60 \text{ pc}$ .

In Figure 8 we show the probability density functions (PDFs) of temperature, (a), and gas density, (b). Each panel features the respective PDFs for models with  $B_0 = 0, 0.5$  and  $5 \mu\text{G}$  at  $t = 2 \text{ Myr}$ . All models have identical initial temperature and gas density distributions. The peaks at  $T \simeq 260 \text{ K}$  and  $\rho \simeq 1.67 \text{ g cm}^{-3}$  identify the ambient ISM. For the HD model and model with  $B_0 = 0.5 \mu\text{G}$ , the differences in the PDFs are otherwise also negligible. The other local maxima identify the cold remnant shell ( $n > 10 \text{ cm}^{-3}, T < 100 \text{ K}$ ), the hot diffuse core ( $n < 0.01 \text{ cm}^{-3}, T > 10^5 \text{ K}$ ), and the accumulation of thermally stable warm gas ( $n \simeq 0.1 \text{ cm}^{-3}, T \simeq 10^4 \text{ K}$ ).

However, with the strong magnetic field the peak temperatures representing the remnant shell and the remnant cores are hotter and more dense. Its magnetically confined hot gas has a smaller fractional volume. Hot gas in all models cools slowly, due to the low density, but the strong MHD hot gas cools due to radiative losses relatively faster due to its slightly higher density. It nevertheless remains hotter, because the adiabatic cooling is reduced. The strong MHD model has almost identical temperature distribution in the range  $10^4 < T < 10^5 \text{ K}$ , although more dense.

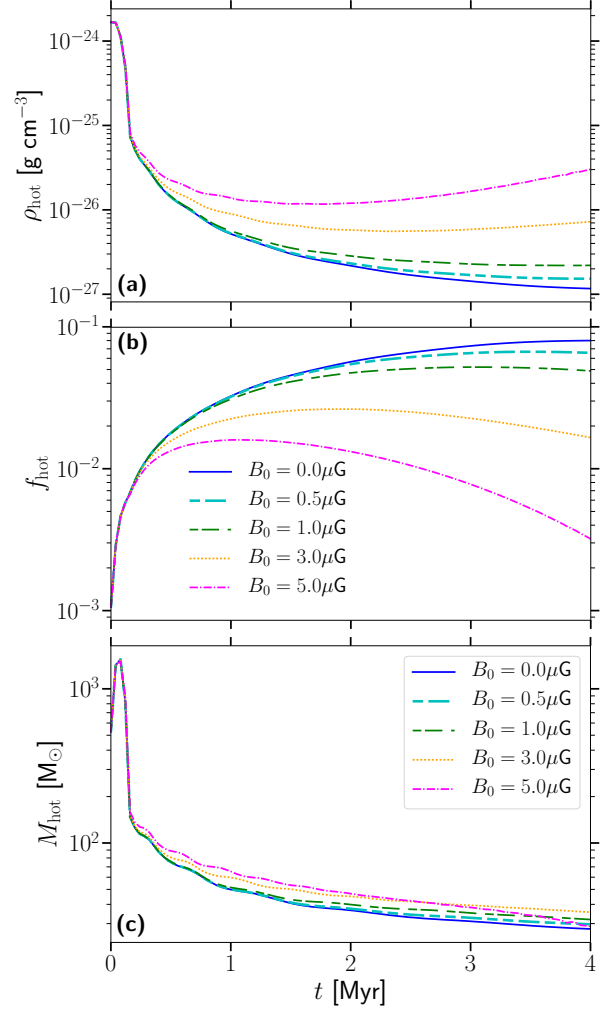


**Figure 9.** Time evolution of (a) mean density of hot gas (b) fractional volume of hot gas (c) mass of hot gas for the HD (solid blue) and MHD models with  $B_0 = 0.5 \mu\text{G}$ . Hot gas is defined as  $T > 2 \cdot 10^4 \text{ K}$  (Kim & Ostriker 2015).

Most unexpected is the large proportion of gas in the MHD model persisting around  $1000 \text{ K}$ . In the HD model below the local maximum at  $10^4 \text{ K}$  is thermally unstable, with gas cooling rapidly to and accumulating at about  $90 \text{ K}$ , where the cooling function,  $\Lambda$ , smoothly truncates. However with a strong magnetic field much of the gas in the remnant persists in this thermally unstable range, the cold peak sustained about  $200 \text{ K}$  and  $n \simeq 2 \text{ cm}^{-3}$ . filling fraction  $\rightarrow$  fractional volume, we went to some lengths in paper 1 to define the three methods of measuring fraction by phase, so let's keep the label precise. Delete when OK The high fractional volume of thermally unstable higher density gas in the MHD model is explained by the revised balance of heating,  $\Gamma$ , and cooling processes, in the inter-shock region illustrated in Figure 7 (b).

Magnetic confinement of hot gas in the remnant is indicated strongly by the increasing mean hot gas density



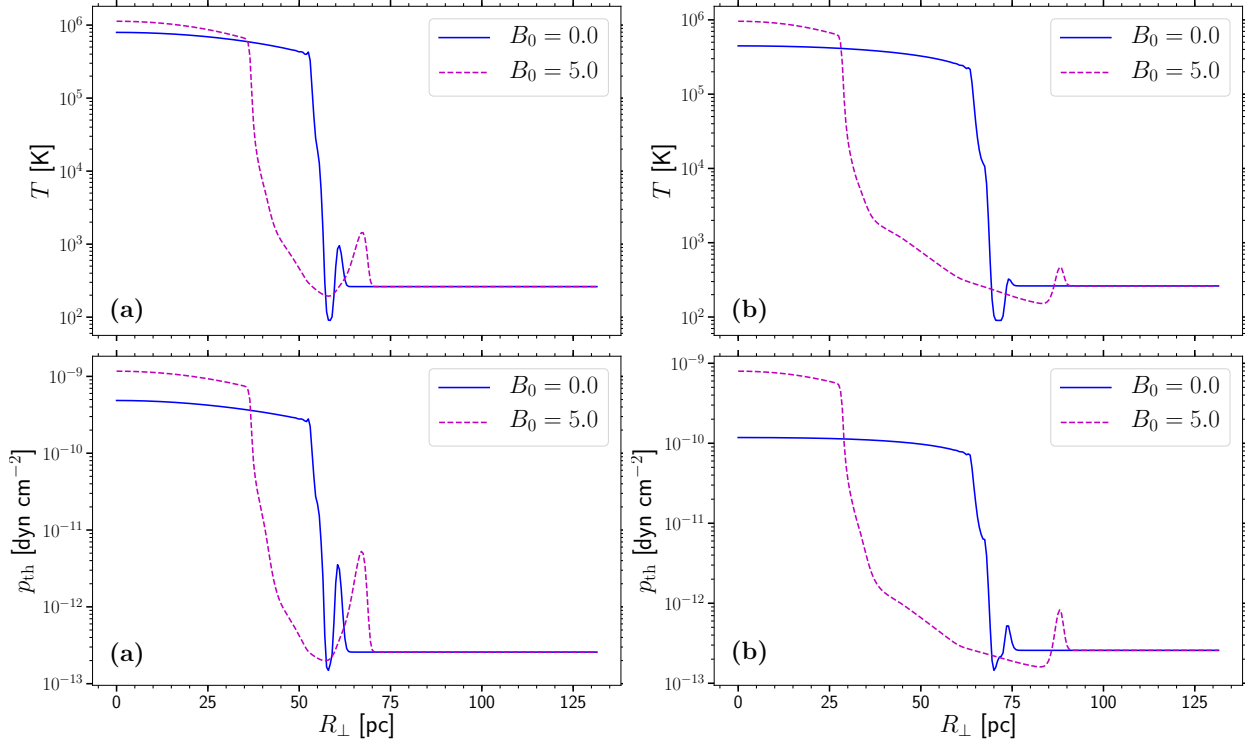


**Figure 10.** Radial profiles at (a) 1 Myr and (b) 2 Myr perpendicular to the magnetic field of gas temperature (top) and thermal pressure (bottom).

plotted in Figure 9 (a) and decreasing fractional volume from Figure 9 (b) of hot gas in strongly magnetized remnants. This effect has also been found in larger-scale simulations of the ISM (Evirgen et al. 2017, 2019). The residual total mass of hot gas deposited into the ISM may be 20–40% greater in the strong MHD remnant as depicted in Figure 9 (c).

In Figure 10 we show radial profiles perpendicular to the magnetic field at 1 Myr (a) and 2 Myr (b), for temperature (top) and thermal pressure (bottom) for the HD and strong MHD remnants. This illustrates the higher temperature in the MHD core, but smaller fractional volume.

## 6. RESIDUAL SN ENERGY INJECTION

Inspection of the momentum injection indicates the magnetic field can reduce the residual momentum applied to the ISM by an SN remnant. The increased mass of hot gas, on the other hand and reduced effect of non-adiabatic cooling within an MHD remnant invites the question how are the energetics of the ISM affected by a strong magnetic field? The time evolution of residual SN total energy and each contribution to the energy are plotted in Figure 11.

Panel (a) shows that a significant increase in residual total energy occurs with strong MHD even within 1 Myr of the supernova explosion.

From Panel (b) we see that the presence of large-scale magnetic fields retains more residual thermal en-

**Table 1.** Energy retention as a percentage of  $E_{\text{SN}}$ , given for each model.

| Time [Myr] | $B_0$ [ $\mu\text{G}$ ] |      |      |      |      |
|------------|-------------------------|------|------|------|------|
|            | 0                       | 0.5  | 1.0  | 3.0  | 5.0  |
| 0.25       | 16.2                    | 16.2 | 16.5 | 17.2 | 18   |
| 0.5        | 10.2                    | 10.3 | 10.4 | 11.4 | 12.4 |
| 1.0        | 5.4                     | 5.5  | 5.9  | 6.7  | 7.7  |
| 2.0        | 2.9                     | 3.1  | 3.5  | 4.6  | 5.5  |
| 4.0        | 1.3                     | 1.6  | 2.0  | 3.5  | 4.2  |

ergy, while Panel (c) shows that kinetic energy in the MHD remnants is lost more quickly. Beyond 3 Myr the strong MHD residual kinetic energy can persist more effectively than HD, would likely be subsumed by the ambient ISM turbulence by this time. For all MHD models there is a modest linear amplification of the magnetic field through compression and tangling (Panel (d)). So the net contributions of thermal and magnetic energy mean that the MHD shocks in fact induce a greater total residual energy into the ISM than HD alone.

The effects are tabulated for each model at various times throughout their evolution in Table 1. Differences emerge with HD within 250 kyr of the SN explosion for

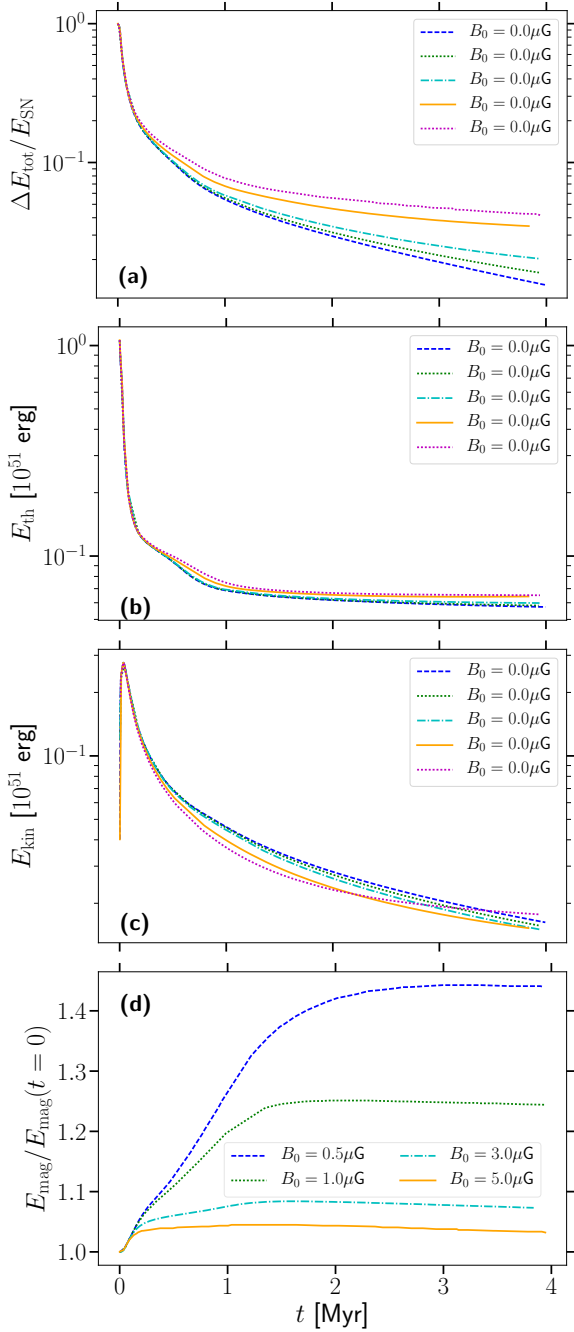


**Figure 11.** (a) Energy retention by HD and MHD ( $5\mu\text{G}$  remnants, where  $\Delta E_{\text{tot}}(t) = E_{\text{tot}}(t) - E_{\text{tot}}(t=0)$ ).  $E_{\text{tot}}(t=0)$  is the total energy in the ambient gas prior to the SN explosion, (b) thermal energy (c) kinetic energy and (d) magnetic energy profiles.

strong MHD models. The  $3\mu\text{G}$  and  $5\mu\text{G}$  models retain 6% and 11% more energy, rising to 10% and 20% within 500 kyr. The HD simulation retains 1.3% of SN energy by the end of the simulation. As magnetic field strength increases, the SN energy retained by the system increases, reaching 4.2% for  $B_0 = 5\mu\text{G}$ .

## 7. CRITICAL MAGNETIC FIELD STRENGTH

Any qualitative differences between the HD and MHD remnants must arise from effects due to the Lorentz force. Inspection of the evolution of magnetic tension reveals this to be negligible, relative to the magnetic and thermal pressure gradients. The maximal tension forces apply in the remnant shell nearest the polar axis of the remnant.

Therefore, modification to momentum injection relies on the interacting radial pressure gradients, particularly where  $\partial_{\perp}(p) \simeq \partial_{\perp}(|\mathbf{B}|^2/2\mu_0)$ . In the blast wave the magnetic gradient will grow due to compression. The stronger the ambient field, the earlier the magnetic gradient in the shell and in its wake will acquire a critical strength sufficient to significantly modify the remnant evolution. The MHD shell begins to shed mass into its wake, compared to HD as early as 200 kyr for  $B_0 = 5\mu\text{G}$ , 320 kyr for  $3\mu\text{G}$  and 920 kyr for  $1\mu\text{G}$ . The leading shock outstrips the HD model at 440, 560 and 1560 kyr, respectively. From both panels in Figure 6 throughout the inter-shock region we have

$$\frac{\partial_{\perp}(|\mathbf{B}|^2/2\mu_0)|_{-}}{\partial_{\perp}(p)|_{+}} \gtrsim 1,$$

but when the MHD shock profiles start to diverge from HD this ratio locally is still much less than 1. A reasonable criteria for identifying the critical large-scale magnetic field strength may be to assume plasma- $\beta < 1$ . Hence,  $B_{\text{crit}} \sim \sqrt{2\mu_0 p}$ , where  $p = k_B n T$ ;  $k_B$  is the Boltzmann constant, and  $T$  denotes temperature.

For these simulations the ambient ISM has  $n = 1 \text{ cm}^{-3}$  and  $T \simeq 260 \text{ K}$ . Thus, the gas is in thermal equilibrium with radiative cooling balancing UV heating. We show in Appendix C that the results are not sensitive to the initial ambient temperature, which cools very quickly to the equilibrium temperature to evolve with the same remnant properties. We obtain  $B_{\text{crit}} \sim 1 \mu\text{G}$ .  $B_0 = 1\mu\text{G}$  does lead to marginal MHD effects. In agreement with Hanayama & Tomisaka (2006), we find that significant change to the nature of the remnant is seen for  $B_0 \geq 3\mu\text{G}$ . However, the effect of cooling and heating processes are highly nonlinear functions of density, so we shall explore how to explain critical field strength with various ambient ISM densities and magnetic field configurations.

## 8. SUMMARY

The merger of the remnant shell with the surrounding gas depends on a number of factors, including but not limited to, ambient sound speed, homogeneity (or inhomogeneity) of the ambient gas density structures, and interaction with other shocks in a turbulent, highly compressible and typically inhomogeneous interstellar medium. However, the emergence of differences in energy retention, directly linked to the presence of large-scale magnetic fields, suggests that the efficiency with

which the surrounding gas extracts energy from SN remnants is modified by magnetic fields.

A plane-parallel, micro-gauss strength magnetic field changes the aspect ratio of SN remnants. The shock-wave through the ambient ISM propagates faster perpendicular to the magnetic field. Figure 15 of [Caunt & Korpi \(2001\)](#) show a similar MHD remnant expanding faster perpendicular to the plane-parallel field. This is also identified by [Ferriere et al. \(1991\)](#) in the context of a superbubble blast wave. They also report that the MHD blast is faster in the parallel direction than for HD. Conversely, the hot diffuse remnant core is magnetically confined into a prolate spheroid with pole aligned to the field. [Hanayama & Tomisaka \(2006\)](#); [Kim & Ostriker \(2015\)](#) also find that expansion of the core is inhibited perpendicular to a plane-parallel magnetic field.

Both effects are caused by the magnetic pressure gradients perpendicular to the magnetic field. In the adiabatic and pressure driven phases of the blast wave expansion, while magnetic forces are weak relative to the explosive forces, magnetic field is expelled from the core and compressed into the shell. Some energy from the thermally driven outward shock is stored in the highly compressed field at the remnant shell, to be released through the magnetic pressure gradient in the late MHD shock. Compression also generates an increasingly negative magnetic pressure gradient just behind the shell, ultimately injecting momentum inwards.

In similar simulations, which focus on the early (up to 400 kyr) stage of SN evolution, [Kim & Ostriker \(2015\)](#) conclude that momentum injection by an SN remnant is unaffected by the presence of a plane-parallel magnetic field. They suggest magnetic fields will not affect momentum injection, because they do not become comparable to thermal effects before the remnant enters the momentum-conserving phase. In contrast we *do* find for  $B_0 \geq 3\mu\text{G}$  a substantial effect on outward momentum injection already within 500 kyr, which could be reduced by up to 10% in the presence of a large-scale magnetic field. Given the role of SN in driving both turbulent and large-scale flows (such as galactic winds), such a reduction in momentum injection could have a noticeable effect on gas dynamics within galaxies.

MHD effects also lead to confinement of the hot core and a more dense inter-shock region. UV-heating exceeds radiative losses in this region and, combined with the magnetic broadening of the shock front, inhibits the formation of cold gas, compared to HD. This results in a region of thermally unstable warm gas, which will eventually merge with the surrounding gas. In contrast to the reduced momentum injection the residual energy of an MHD SN remnant can be up to 40% greater within 1 Myr. This, however, corresponds to a reduced fractional volume of hot gas, an effect also noted by [Evirgen et al. \(2019\)](#). Even though we obtain this result in an idealized numerical setup, [Evirgen et al. \(2019\)](#) find that hot gas becomes more dense in numerical simula-

tions of the local Galaxy, as the magnetic field reaches  $B_{\text{rms}} \sim 3\mu\text{G}$  strength with a strong large-scale component. These numerical simulations feature highly inhomogeneous gas density, compressible turbulence and a multi-phase ISM structure. Thus, it is plausible that our remnant-scale simulations may relate to magnetic effects found in more sophisticated numerical models.

In its early stages the presence of a magnetic field has negligible effect on SN remnant evolution, and this is consistent with the results of [Kim & Ostriker \(2015\)](#). However, as the magnetic shell forms increasingly strong local pressure gradients the dynamics alter markedly. For sufficiently weak magnetic fields this may evolve so late that the blast wave has already merged with the ISM and it remains dynamically insignificant. For stronger fields the magnetic retrograde shock and late MHD shock occur sufficiently early to alter remnant momentum injection and structure. For gas density  $n = 1\text{cm}^{-3}$ , we find the critical field strength to correspond to plasma- $\beta = 1$  in the ambient ISM. The magnetic confinement and late MHD shock occur earlier and are stronger as  $B_0$  increases within the range  $1 \leq B_0 \leq 5\mu\text{G}$  considered. With respect to structure, this is consistent with [Hanayama & Tomisaka \(2006\)](#), who find noticeable magnetic confinement of the remnant interior for  $B_0 \geq 3\mu\text{G}$ , and [Kim & Ostriker \(2015\)](#) for  $B_0 = 7.2\mu\text{G}$ .

Magnetic fields in the ISM are not uniform as applied in these models and planned studies shall include the effects of turbulent structure of the magnetic field and a range of ambient ISM density. Nevertheless, it is widely observed that spiral galaxies have a large-scale, coherently structured magnetic field of strength in the range  $1\text{--}30\mu\text{G}$  ([Beck 2001](#); [Tabatabaei et al. 2008](#); [Fletcher et al. 2011](#)). Thus, it is plausible that SN remnants evolve subject to the magnetic effects described here, which could have significant implications on pressure support, mass loading of the galactic halo, and generally the multiphase and vertical structure of the ISM.

## ACKNOWLEDGEMENTS

We would like to thank the referee for their insightful feedback, which has helped improve both the scientific content and narrative of this Paper.

The work has been performed under the Project HPC-EUROPA3 (INFRAIA-2016-1-730897), with the support of the EC Research Innovation Action under the H2020 Programme; in particular, CCE gratefully acknowledges the support of the Department of Computer Science at Aalto University and the computer resources and technical support provided by the CSC HPC Centre in Finland. FAG acknowledges financial support of the Grand Challenge project SNDYN and GDYNS, CSC-IT Center for Science Ltd. (Finland) and the Academy of Finland Project 272157.

## REFERENCES

- Alves, M. I. R., Boulanger, F., Ferrière, K., & Montier, L. 2018, *A&A*, 611, L5, doi: [10.1051/0004-6361/201832637](https://doi.org/10.1051/0004-6361/201832637)
- Beck, R. 2001, *SSRv*, 99, 243
- Cardillo, M., Tavani, M., Giuliani, A., et al. 2014, *A&A*, 565, A74, doi: [10.1051/0004-6361/201322685](https://doi.org/10.1051/0004-6361/201322685)
- Caunt, S. E., & Korpi, M. J. 2001, *A&A*, 369, 706, doi: [10.1051/0004-6361:20010157](https://doi.org/10.1051/0004-6361:20010157)
- Chevalier, R. A. 1974, *ApJ*, 188, 501, doi: [10.1086/152740](https://doi.org/10.1086/152740)
- Chevalier, R. A., & Clegg, A. W. 1985, *Nature*, 317, 44, doi: [10.1038/317044a0](https://doi.org/10.1038/317044a0)
- Cioffi, D. F., McKee, C. F., & Bertschinger, E. 1988, *ApJ*, 334, 252, doi: [10.1086/166834](https://doi.org/10.1086/166834)
- de Gasperin, F., Evoli, C., Brüggen, M., et al. 2014, *A&A*, 568, A107, doi: [10.1051/0004-6361/201424191](https://doi.org/10.1051/0004-6361/201424191)
- Evirgen, C. C., Gent, F. A., Shukurov, A., Fletcher, A., & Bushby, P. 2017, *MNRAS*, 464, L105, doi: [10.1093/mnras/rlw196](https://doi.org/10.1093/mnras/rlw196)
- Evirgen, C. C., Gent, F. A., Shukurov, A., Fletcher, A., & Bushby, P. J. 2019, in press, arXiv:1903.10263. <https://arxiv.org/abs/1903.10263>
- Ferriere, K. M., Mac Low, M.-M., & Zweibel, E. G. 1991, *ApJ*, 375, 239, doi: [10.1086/170185](https://doi.org/10.1086/170185)
- Fletcher, A., Beck, R., Shukurov, A., Berkhuijsen, E. M., & Horellou, C. 2011, *MNRAS*, 412, 2396, doi: [10.1111/j.1365-2966.2010.18065.x](https://doi.org/10.1111/j.1365-2966.2010.18065.x)
- Gent, F. A. 2012, PhD thesis, Newcastle University School of Mathematics and Statistics
- Gent, F. A., Mac Low, M.-M., Käpylä, M. J., Sarson, G. R., & Hollins, J. F. 2019, *GAFD*, in press, arXiv:1806.01570. <https://arxiv.org/abs/1806.01570>
- Gent, F. A., Shukurov, A., Fletcher, A., Sarson, G. R., & Mantere, M. J. 2013, *MNRAS*, 432, 1396, doi: [10.1093/mnras/stt560](https://doi.org/10.1093/mnras/stt560)
- Girichidis, P., Walch, S., Naab, T., et al. 2016, *MNRAS*, 456, 3432, doi: [10.1093/mnras/stv2742](https://doi.org/10.1093/mnras/stv2742)
- Hanayama, H., & Tomisaka, K. 2006, *ApJ*, 641, 905, doi: [10.1086/500527](https://doi.org/10.1086/500527)
- Hawley, J. F., Smarr, L. L., & Wilson, J. R. 1984, *ApJ*, 277, 296, doi: [10.1086/161696](https://doi.org/10.1086/161696)
- Jun, B.-I., & Norman, M. L. 1996, *The Astrophysical Journal*, 472, 245
- Kim, C.-G., & Ostriker, E. C. 2015, *ApJ*, 802, 99, doi: [10.1088/0004-637X/802/2/99](https://doi.org/10.1088/0004-637X/802/2/99)
- Mac Low, M.-M., & Klessen, R. S. 2004, *Reviews of Modern Physics*, 76, 125, doi: [10.1103/RevModPhys.76.125](https://doi.org/10.1103/RevModPhys.76.125)
- McKee, C. F., & Ostriker, J. P. 1977, *ApJ*, 218, 148, doi: [10.1086/155667](https://doi.org/10.1086/155667)
- Murray, N., Quataert, E., & Thompson, T. A. 2005, *ApJ*, 618, 569, doi: [10.1086/426067](https://doi.org/10.1086/426067)
- Sarazin, C. L., & White, III, R. E. 1987, *ApJ*, 320, 32, doi: [10.1086/165522](https://doi.org/10.1086/165522)
- Sedov, L. I. 1959, *Similarity and Dimensional Methods in Mechanics*
- Slavin, J. D., & Cox, D. P. 1992, *ApJ*, 392, 131, doi: [10.1086/171412](https://doi.org/10.1086/171412)
- Sod, G. A. 1978, *Journal of Computational Physics*, 27, 1, doi: [10.1016/0021-9991\(78\)90023-2](https://doi.org/10.1016/0021-9991(78)90023-2)
- Spitzer, L. 1978, *Physical processes in the interstellar medium*, doi: [10.1002/9783527617722](https://doi.org/10.1002/9783527617722)
- Tabatabaei, F. S., Krause, M., Fletcher, A., & Beck, R. 2008, *A&A*, 490, 1005, doi: [10.1051/0004-6361:200810590](https://doi.org/10.1051/0004-6361:200810590)
- Taylor, G. 1950, *Proceedings of the Royal Society of London Series A*, 201, 159, doi: [10.1098/rspa.1950.0049](https://doi.org/10.1098/rspa.1950.0049)
- Tomisaka, K. 1998, *MNRAS*, 298, 797, doi: [10.1046/j.1365-8711.1998.01654.x](https://doi.org/10.1046/j.1365-8711.1998.01654.x)
- Tomisaka, K., Habe, A., & Ikeuchi, S. 1981, *Ap&SS*, 78, 273, doi: [10.1007/BF00648941](https://doi.org/10.1007/BF00648941)
- Wolfire, M. G., Hollenbach, D., McKee, C. F., Tielens, A. G. G. M., & Bakes, E. L. O. 1995, *ApJ*, 443, 152, doi: [10.1086/175510](https://doi.org/10.1086/175510)
- Yadav, N., Mukherjee, D., Sharma, P., & Nath, B. B. 2017, *MNRAS*, 465, 1720, doi: [10.1093/mnras/stw2522](https://doi.org/10.1093/mnras/stw2522)
- Zirakashvili, V. N., & Ptuskin, V. S. 2008, *The Astrophysical Journal*, 678, 939

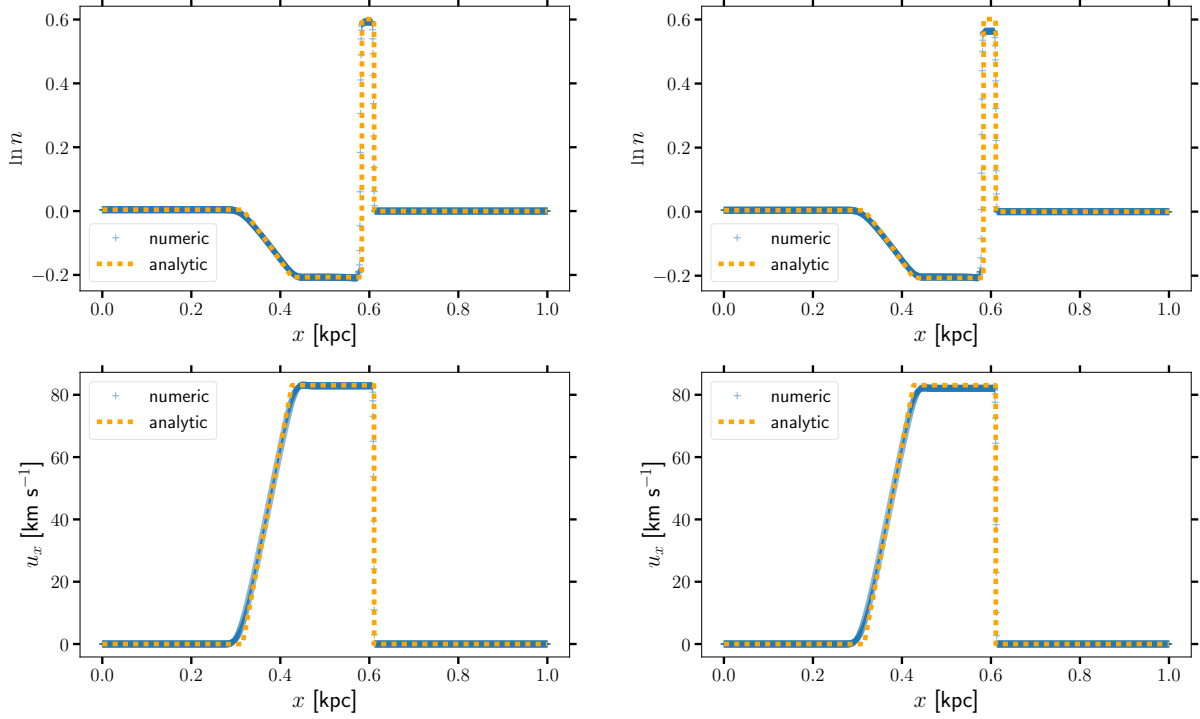


**Figure 12.** Shock-tube simulations for HD (left panels) and MHD (right panels) with  $\nu$  and  $\eta$  as applied to the 3D simulations. The spatial resolution is 0.5 pc. The MHD simulation features a  $5\mu\text{G}$  uniform magnetic field perpendicular to the shock tube. Upper panels show log gas number density and lower panels gas velocity at  $t = 1$  Myr.

## APPENDIX

### A. IDENTIFYING NUMERICAL EFFECTS THROUGH 1D SHOCK-TUBE TESTS

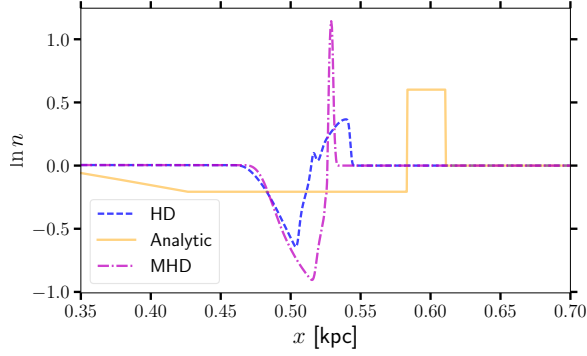
To verify that the significant qualitative effects we identify from the MHD blast waves are attributable to the physics rather than the numerics, we examine the impact of employing artificial diffusivities compared to the impact of a magnetic field on the solutions. For numerical economy we use a set of 1D shock-tube tests. The numerical solutions for adiabatic shocks with parameters relevant to SN blast waves are compared to the system originally described by Sod (1978), and its exact analytical solution derived by Hawley et al. (1984). We extend the analysis applied to the HD solutions of Gent et al. (2019) to consider specifically whether MHD or numerical effects account for the differences in the MHD solutions.

Figure 12 shows that for an adiabatic shock the HD numerical solution reliably produces the analytic solution. Even the MHD solution has only marginally enhanced gas density in the shock. Hence, neither numerical parameters nor the presence of the magnetic field have a significant effect on the solution in the adiabatic system, and this is consistent with most previous assessments.

We next consider the effect radiative cooling and UV heating on the shock-tube solution. In Figure 13 the non-adiabatic HD and MHD numerical solutions are contrasted to the adiabatic analytic solution. We do not have a non-adiabatic analytic shock-tube solution. The inclusion of cooling and heating processes has a noticeable effect on both HD and MHD shock tubes; both shocks propagate more slowly through the ambient gas. This is not unexpected, since these processes extract energy which would otherwise be used up in the propagation of the shock. We note that the MHD shock propagates faster than the HD shock, as also seen in the 3D simulations presented in this Paper. The gas density behind the shock tube is higher than the standard set up for both HD and MHD shock tubes with cooling and heating. However, as seen in the 3D simulations, the gas density is higher behind the shock for the MHD shock tube. In addition, the shock density is lower in the MHD shock. This is evidence that the nonlinear interaction between the MHD and non-adiabatic effects is a significant factor in the divergence of the HD and MHD solutions.

For the 1D shock-tube tests an artificial shock-dependent mass diffusion is unnecessary, but we include it in these experiments to verify that its inclusion in SN-driven turbulence simulations does not induce excessive numerical diffusion. We consider a range of mass shock diffusivity  $\zeta_D \in [0, 10]f_{\text{shock}}$ . From Figure 14 we show that adding mass





**Figure 13.** Comparison of the numerical non-adiabatic HD and MHD shock-tube solutions, alongside the adiabatic analytic solution.

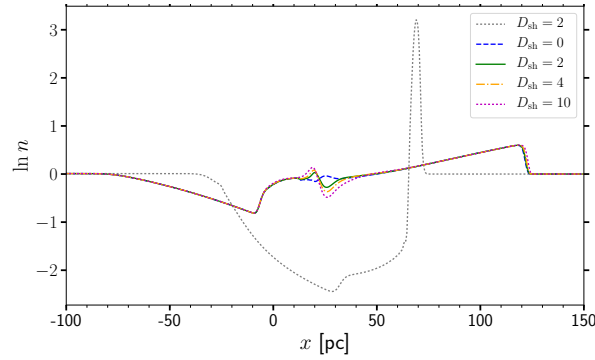


**Figure 14.** The non-adiabatic MHD shock-tube solution is contrasted with its HD solution for a range of mass diffusion rates,  $\zeta_D = [0, 2, 4, 10]f_{\text{shock}}$ .

diffusion, while providing numerical stability, produces a minor quantitative difference in the gas density shock profile. The profiles are otherwise qualitatively the same and the contrast with the HD profile is clearly down to the presence of the magnetic effects rather than the mass diffusion. A remaining concern is that the broadening of the mass profile in the MHD blast wave may arise from the high value of the viscosity,  $\nu = \nu_0$  with  $\nu_0 = 0.0005c_s \text{ kpc km s}^{-1}$  in the 3D SN blast waves. Although the estimates of microscopic viscosity in the real ISM are orders of magnitude lower, the viscosity in the model represents instead a turbulent viscosity. To model turbulence we require this dissipation scale applies above the grid scale, but sufficiently below the SN forcing scale to accurately capture the energy spectrum down to the smallest scales of interest in the model. We vary  $\nu = [\nu_0, 2\nu_0, 4\nu_0, 8\nu_0, 16\nu_0]$  with  $\zeta_D = 2f_{\text{shock}} \text{ kpc km s}^{-1}$  and  $\eta = 0.0008 \text{ kpc km s}^{-1}$  for the non-adiabatic 1D shock-tube tests. This also effectively changes the magnetic Prandtl number in the MHD simulations, defined as  $P_m = \nu/\eta$ , which yields  $P_m = [0.625, 1.25, 2.5, 5, 10]c_s$ . Given that in these solutions  $c_s \gg 1 \text{ km s}^{-1}$ , we also have  $P_m \gg 1$ .

Some resulting density profiles are shown in Figure 15. Both HD and MHD are affected similarly by increasing viscosity. The shock front does not propagate as fast for higher values of  $\nu$  and the region behind the shock is smoothed. However both HD and MHD shocks are not affected qualitatively as viscosity is increased. The difference between the HD and MHD solutions cannot be explained by high diffusivity.

## B. CHANGING THE AMBIENT GAS DENSITY

There is a significant change to the HD SN evolution when a moderately strong uniform magnetic field is embedded in the ambient ISM. We conclude that this is in part due to the alteration of the radiative cooling and UV-heating characteristics in response to the retrograde flow of gas into the remnant. The cooling and heating profile of the ISM is highly sensitive to the gas density and temperature. We would like to explore the response to varying ambient ISM density in the 3D MHD SN remnant evolution in future work, but here we perform a preliminary low budget experiment with 1D shock-tube tests of varying ambient gas density. We apply ambient gas number density,  $n_0 = 10^{-2}, 10^{-1}, 1, 10, 100 \text{ cm}^{-3}$  to assess whether the magnetic effects described in this Paper may be generalised beyond  $1 \text{ cm}^{-3}$ . The range of densities chosen reflect the range from diffuse, hot gas to dense, cold gas. The initial entropy of

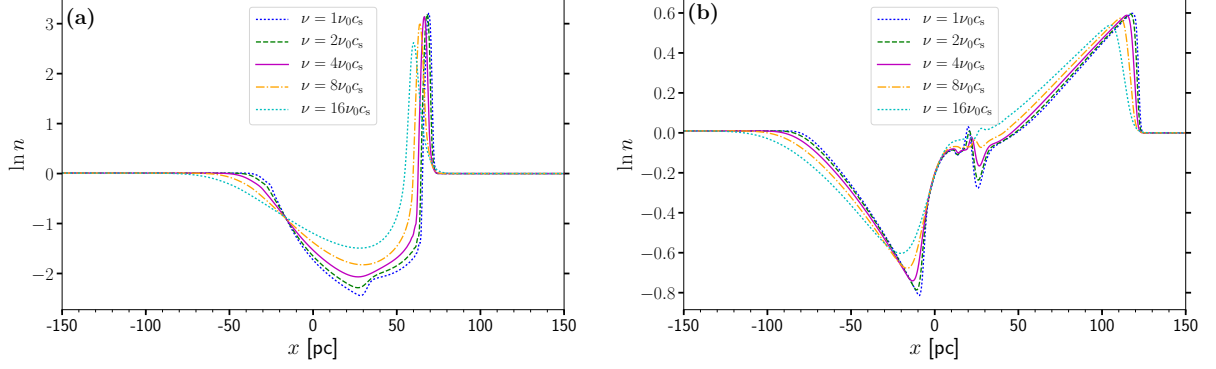


**Figure 15.** HD (left) and MHD (right) non-adiabatic shock-tube solutions for  $\nu \in [\nu_0, 2\nu_0, 4\nu_0, 8\nu_0, 16\nu_0]$ .

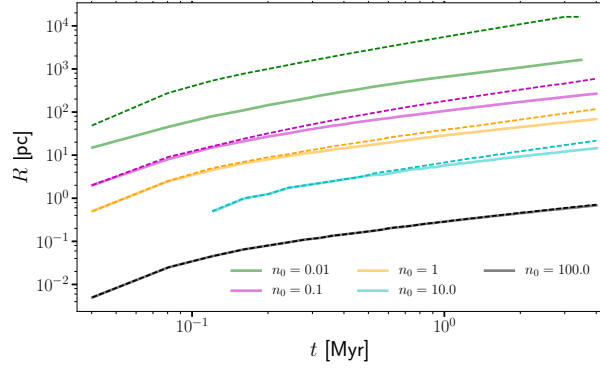


**Figure 16.** Shock radius for 1D non-adiabatic MHD shock-tube simulations ( $B_0 = 5\mu\text{G}$ ), for a range of ambient gas densities. Solid lines indicate the profiles for HD models at the given background density, while dashed lines of the same colour represent MHD models of the same background density.

the ambient gas is adjusted such that the ambient temperature remains constant with net heating at zero appropriate to the initial gas density. Specific gas entropy is expressed as

$$s = c_V [\ln T - (\gamma - 1) \ln \rho],$$

with  $T$  and  $\rho$  expressed in dimensionless code units,  $\gamma = 5/3$  is the adiabatic index, and  $c_V$  is the specific heat capacity. Some initial configuration is represented by  $T_0$ ,  $\rho_0$  and,

$$s_0 = c_V [\ln T_0 - (\gamma - 1) \ln \rho_0].$$

We change the gas density such that  $\rho_1 = k\rho_0$ , where  $k > 0$ , but keep the temperature constant, such that  $T_0 = T_1$ . The two entropies, the new entropy  $s_1$  can be related to the old value  $s_0$ :

$$\begin{aligned} s_1 &= s_0 + c_V(\gamma - 1) [\ln \rho_0 - \ln k\rho_0], \\ s_1 &= s_0 + c_V(1 - \gamma) \ln k. \end{aligned} \tag{B1}$$

We use this expression to change gas density while keeping initial temperature constant. In Figure 16, we present the time profiles of distance travelled by the non-adiabatic shock (analogous to remnant shell radius) for a range of ambient gas densities. The effect of the magnetic field is measured by the difference between the profiles for HD and MHD shocks of identical ambient gas density. As in the 3D SN simulations, divergence of the MHD shock profile from the HD profile indicates the effect of magnetic field. We find that the effect of the magnetic field increases as the ambient density becomes more diffuse, due to decreasing plasma- $\beta$ . Magnetic effects are seen for all ambient densities apart from  $n = 100 \text{ cm}^{-3}$ . Magnetic effects appear earlier in the lower ambient gas densities.

### C. TEMPERATURE OF THE AMBIENT GAS

In our simulations, we set the ambient gas temperature  $T_0 = 260 \text{ K}$ , to ensure that the SN explosion is set off with an ambient medium in thermal equilibrium. This particular temperature is chosen as the radiative cooling and

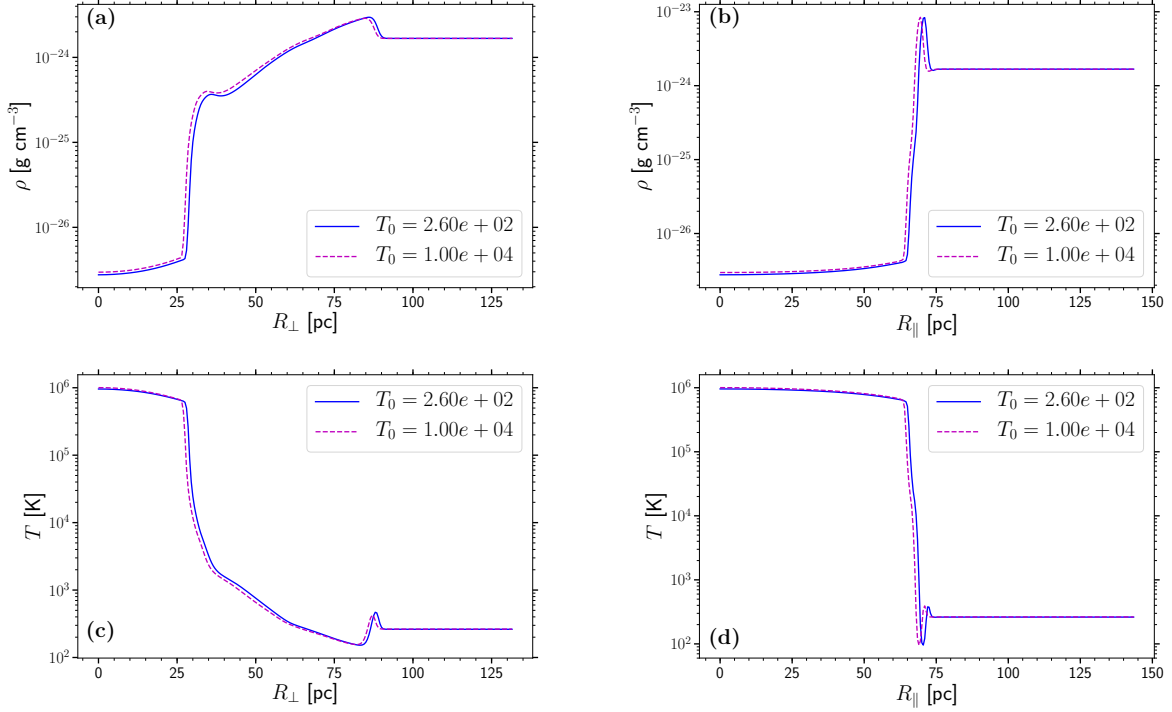


**Figure 17.** Radial profiles of gas temperature (top row) and density (bottom row) perpendicular (left column) and parallel (right column) to the magnetic field. The radial profiles shown here are taken at  $t = 2$  Myr.

UV-heating balance each other, yielding zero net heating in the ambient gas. However,  $T_0 \sim 10^4$  K is a more typical temperature for the ISM, particularly for ambient gas number density,  $n_0 \sim 0.1 \text{ cm}^{-3}$ . Using this low density would substantially increase the numerical domain size and computational expense. We, therefore, run a 3D SN simulation identical to the MHD remnant simulation with  $B_0 = 5 \mu\text{G}$  and  $n_0 = 1 \text{ cm}^{-3}$ , but with  $T_0 = 10^4$  K.

Figure 17 shows that the radial profiles of gas density and temperature are qualitatively identical and quantitatively very similar at 2 Myr. The re-distribution of mass from the shell to the interior of the remnant occurs in both models, forming the inter-shock region between the magnetically confined diffuse core and the shell, in the direction perpendicular to the magnetic field.

Moreover, the PDFs of gas temperature and density provided in Figure 18, which are given at 400 kyr, 1 Myr and 2 Myr, show that the temperature distributions converge despite the different initial temperatures. The hottest gas is identical from an early stage, as it is injected by the SN remnant, irrespective of the initial ambient gas temperature. In the cooler range, the modal temperature of the gas, for the  $10^4$  K model, gradually converges to the 260 K model, for which the ambient gas is in thermal equilibrium from the beginning of the simulation. We see that the lower peak in the temperature PDF, corresponding to the ambient ISM, cools over time, reaching thermal equilibrium peak by 2 Myr. Evidently, the difference to the thermal pressure gradient from the higher temperature is negligible.

Figure 19 shows the evolution of remnant radius perpendicular and parallel to the magnetic field. Panel (b) shows that the HD model and both MHD models agree with the [Cioffi et al. \(1988\)](#) analytical solution. The radius of the  $10^4$  K MHD model is marginally (within 2 pc) less than the 260 K model. Panel (a) shows that both MHD models have an identical time profile for the radius perpendicular to the magnetic field.

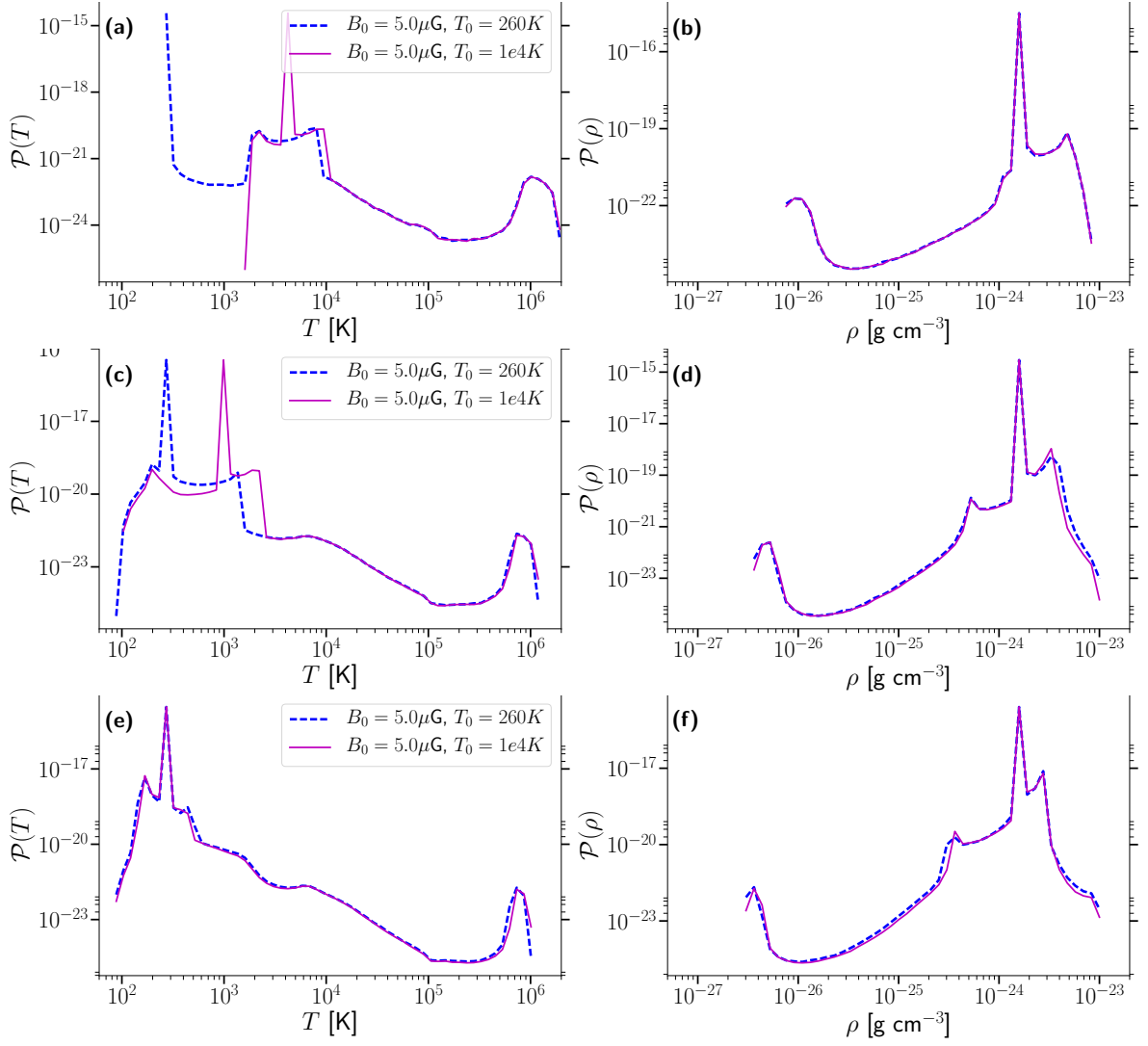


**Figure 18.** PDFs of gas temperature (left column) and gas density (right column) for the MHD model ( $B_0 = 5 \mu\text{G}$ ) with initial ambient gas temperatures of 260 K and  $10^4$  K, at 400 kyr (top row), 1 Myr (middle row), and 2 Myr (bottom row)

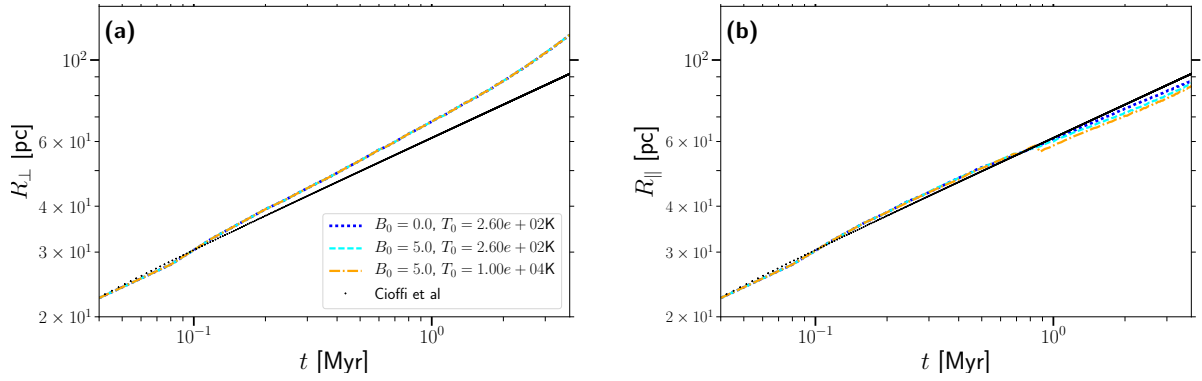


**Figure 19.** Time profile of the remnant radius (a) perpendicular and (b) parallel to the magnetic field. We compare the HD remnant, MHD remnant with both  $T_0 = 260$  K and  $T_0 = 10^4$  K, with the Cioffi et al. (1988) analytical solution.